Biomech Model Mechanobiol (2014) 13:679–695
DOI 10.1007/s10237-013-0527-7

ORIGINAL PAPER

Effects of wall distensibility in hemodynamic simulations of an arteriovenous fistula

Patrick M. McGah · Daniel F. Leotta · Kirk W. Beach · Alberto Aliseda

Received: 10 May 2013 / Accepted: 30 August 2013 / Published online: 15 September 2013

Abstract Arteriovenous fistulae are created surgically to provide adequate access for dialysis patients suffering from end-stage renal disease. It has long been hypothesized that the rapid blood vessel remodeling occurring after fistula creation is in part a process to restore the mechanical stresses to some preferred level, i.e., mechanical homeostasis. The current study presents fluid–structure interaction (FSI) simulations of a patient-specific model of a mature arteriovenous fistula reconstructed from 3D ultrasound scans. The FSI results are compared with previously published data of the same model but with rigid walls. Ultrasound-derived wall motion measurements are also used to validate the FSI simulations of the wall motion. Very large time-averaged shear stresses, 10–15 Pa, are calculated at the fistula anastomosis in the FSI simulations, values which are much larger than what is typically thought to be the normal homeostatic shear stress in the peripheral vasculature. Although this result is systematically lower by as much as 50 % compared to the analogous rigid-walled simulations, the inclusion of distensible vessel walls in hemodynamic simulations does not reduce the high anastomotic shear stresses to "normal" values. Therefore, rigid-walled analyses may be acceptable for identifying high shear regions of arteriovenous fistulae.

Keywords Vascular remodeling · Hemodynamics · Dialysis access · End-stage renal disease

Electronic supplementary material The online version of this article (doi:10.1007/s10237-013-0527-7) contains supplementary material, which is available to authorized users.

This work has been financially supported by an R21 grant from NIDDK (DK08-1823), a graduate student fellowship from the Washington NASA Space Grant Consortium (NASA Grant NNX10AK64H), a NSF CAREER Award (CBET-0748133), and a Washington Royalty Research Fund grant.

P. M. McGah (✉) · A. Aliseda
Department of Mechanical Engineering, University of Washington, Seattle, WA 98115, USA
e-mail: pmcgah@u.washington.edu

A. Aliseda
e-mail: aaliseda@u.washington.edu

D. F. Leotta
Applied Physics Laboratory, Center for Industrial and Medical Ultrasound, University of Washington, Seattle, WA 98195, USA

K. W. Beach
Department of Surgery, University of Washington, Seattle, WA 98195, USA

K. W. Beach
Department of Bioengineering, University of Washington, Seattle, WA 98195, USA

1 Introduction

Hemodialysis is a common treatment for approximately 370,000 patients in the USA with end-stage renal disease or ESRD (US Renal Data System 2012). To optimize the procedure, the dialysis access site must be easily accessible but must also be able to continuously provide high blood flow rates, usually > 250 mL/min (Tordoir et al. 2003), to the dialyzer. If there is insufficient blood flow through the access, then dialysis becomes impractical or ineffective. To provide these two combined features, which are not found together in the human circulation, an arteriovenous (AV) fistula is typically created surgically in the arm: an artery, usually the radial, and a vein, usually the cephalic, are anastomosed together, bypassing the high flow resistance of the capillary bed in the hand and providing enhanced flow through the artery and into the access vein.

Unfortunately, as many as 60 % of AV fistulae will either fail or require an intervention within one year to maintain clinical patency (Gibson et al. 2001; Lauvao et al. 2009). There are two major causes of patency loss: 1) occlusion, brought on by aggressive intimal hyperplasia, and 2) impaired dilation, whereby venous outward remodeling is not sufficient to provide a high flow rate at the access site (Tordoir et al. 2003). In the USA alone, it is estimated that the total health care expenditures related to access site complications and revisions amount to about $2 billion per year (US Renal Data System 2012). Perhaps most striking is the fact that ESRD patients in the USA represent 1.3 % of all Medicare patients, yet the total annual Medicare expenditures for ESRD treatments are $33 billion accounting for 7.9 % of all annual Medicare expenditures.

After the creation of the fistula, the vein undergoes a rapid remodeling process typically lasting 12–16 weeks (Wong et al. 1996). The venous lumen will often double in diameter (Shemesh et al. 2007), and the venous wall will increase in thickness and muscular tone (Kritharis et al. 2010). It has long been hypothesized that hemodynamic forces constitute the primary external influence on the remodeling process (Kamiya and Togawa 1980; Zarins et al. 1987). Since an AV fistula causes a dramatic rise in flow rate, oftentimes more than a 20-fold increase, the wall shear stress is initially elevated to values outside of a normal physiological range (Corpataux et al. 2002). Therefore, it is in turn hypothesized that the vein and artery lumens increase, both acutely and chronically, as a way to renormalize the value of the viscous wall shear stress. Indeed, the remodeling of the vessels has been shown to correlate with the initial time-averaged wall shear stress as evidenced by animal models of AV fistulae (Kamiya and Togawa 1980; Zarins et al. 1987) and ultrasound surveillance in dialysis patients (Corpataux et al. 2002; Girerd et al. 1996). These studies hypothesized that the rapid remodeling phase stops once the mean wall shear stress in the fistulae reaches about 1.5 Pa in the radial artery and about 1.0 Pa in the cephalic vein. The renormalization of shear stress in the fistula vessels has been interpreted as evidence of a "mechanical homeostasis" (Humphrey 2008): the vessels seek to maintain a preferred mechanical state through a process of growth and remodeling. Shear-induced remodeling is widely hypothesized to be regulated in part by the vascular endothelium (Owens et al. 2010).

Despite the pervasive use of the AV fistula for dialysis access, the mechanisms which drive a fistula to either maturation versus occlusion and failure remain obscure (Dixon 2006). Even though blood flow is thought to play an important role in fistula remodeling, the characterization of either beneficial or detrimental hemodynamic stresses occurring within fistulae remains ambiguous (Carroll et al. 2011; Ene-Iordache and Remuzzi 2012; Krishnamoorthy et al. 2008).

In prior work (McGah et al. 2013), we reported that the wall shear stresses in four patient-specific computational models of fistulae were well above what is typically considered the homeostatic value; much of the anastomotic lumens were subjected to ≥ 15 Pa for most of or even all of the cardiac cycle due to the complex shape of the anastomosis and the relatively high flow velocities. However, the fistulae were all over two years old, which is much longer than the initial rapid remodeling phase, and were clinically patent at the time of the imaging. Thus, the non-homeostatic shear stress values did not appear to hinder fistula clinical utility. However, previous studies have assumed rigid walls in all cases.

Motivated by the results of McGah et al. (2013), we studied computational fluid–structure interaction (FSI) to investigate the role of vascular wall distensibility in altering hemodynamic stresses within a 3D ultrasound-derived patient-specific model of an arteriovenous fistula. The previously reported rigid-wall simulations are used as a baseline comparison. Additionally, it has long been hypothesized that the mismatch of elastic properties between the vein and artery at the anastomosis causes increased strain, leading to cellular proliferation and intimal hyperplasia (Bassiouny et al. 1992). Therefore, we also aim to quantify the cyclic wall strain in the fistula. There have been no computational investigations of fully coupled, 3D fluid–structure interaction of arteriovenous fistulae to date. This study, therefore, represents an improvement in the understanding of hemodynamics and biomechanics of hemodialysis access sites.

2 Methods

Patient data of an AV fistulae in the forearm used for dialysis access are examined in this study. The data were collected via 3D and Doppler ultrasound with a protocol approved by the University of Washington Institutional Review Board. The fistula was 7.6 years from time of surgical creation to time of ultrasound examination and was fully functional for dialysis access at the time when the data of this study were collected. The fistula is an end-to-side anastomosis configuration where the cephalic vein is excised and its proximal end is connected to the side of the radial artery. Blood pressure was recorded with a sphygmomanometer over the radial artery on the arm opposite of the fistula.

Vessel imaging was performed with a custom three-dimensional ultrasound imaging system that has been described in detail elsewhere (Leotta et al. 2001, 2003). Briefly, a magnetic tracking system (Flock of Birds, Ascension Technology, Burlington, VT) provides measurements of the location and orientation of the ultrasound scanhead during the examination. The ultrasound imager (SonixTouch, Ultrasonix Medical Corporation, Richmond, BC, Canada) and magnetic tracking system are interfaced with a personal

computer equipped with custom software for simultaneous acquisition of the ultrasound images and the associated location data.

Three types of data were acquired: 1) three-dimensional shape of the artery, anastomosis, and vein, 2) Doppler blood velocity spectral waveform data, 3) wall motion measurements along the artery and vein. The 3D configuration of the vessels was acquired by continuously capturing a series of cross-sectional 2D grayscale images at a rate of 30 frames/s as the scanhead is manually swept along the vessels of interest. The scanhead is swept at a rate of about 5–10 mm/s. Spectral Doppler waveforms are also recorded at several locations in the proximal vessels and in the anastomoses. The spectral Doppler system records the distribution of blood velocities over time (at 10 ms intervals) at selected regions within a vessel. Each wall motion measurement was acquired by capturing a 3-second sequence of 2D images of the vessel lumen at 30 frames per second with the scanhead held stationary over the segment of interest. The image sequence is then reformatted to show the motion from a single scan. The local diameter and the local wall thickness of the vessel in the region of interest were calculated in a post-processing step using the software Carotid Analyzer (Medical Imaging Applications LLC, Coralville, IA). The reproducibility is $\pm 70\,\mu\text{m}$ for both the time-dependent diameter measurements and the wall thickness measurements.

To create a 3D model of the fistula, the vessel lumen was segmented on a subset of the captured images using custom software (Legget et al. 1998). Additional custom software within MATLAB (The MathWorks, Natick, MA) was used to reconstruct 3D surfaces from cross-sectional outlines (Leotta et al. 2001). The software connects the contour points using B-splines to generate a 3D surface model. The reproducibility in the cross-sectional areas of the reconstructed vessels and anastomoses has been determined to be within $\pm 2.4\,\text{mm}^2 (\approx 10\,\%)$ (Leotta et al. 2003). The suture line of the fistula, which denotes where the arterial and venous tissue meet, is manually outlined on the 3D surface model. A previous study demonstrated that the manual identification of the suture line is reproducible to within 2–3 % with respect to the total suture line perimeter (Leotta et al. 2005).

2.1 Material model

As a preliminary step for the following analysis, the Lagrangian reference configuration of the solid vessel wall is taken to be *that of the vessel obtained from the ultrasound imaging* which represents the position of the vessel lumen time-averaged over the cardiac cycle. Although fluid–structure interaction simulations in the cardiovascular system are very challenging numerically (Taylor and Figueroa 2009), additional simplifications can be made in the AV fistula studied here. The coupled fluid–solid problem can be suitably linearized when certain conditions are satisfied such as small deformations; radial deformations are typically as low as 1–2 % in the normal brachial artery (Dammers et al. 2003).

In the classical theory of linear elasticity, the reference configuration is chosen to be stress free (Gurtin et al. 2010). However, that is not the case here as blood vessels in situ are known to be in a mechanically stressed state (Humphrey 2002). Therefore, special consideration must be taken during the linearization procedure. For a given solid body, the position vectors $\mathbf{X}$ and $\mathbf{x}(\mathbf{X}, t)$ denote the reference and current positions, respectively. The displacement vector is denoted as $\boldsymbol{\eta}(\mathbf{X}, t)$, and the displacement gradient tensor is denoted as $\mathbf{H}(\mathbf{X}, t)$. The linearization of the equations of motion for the body is appropriate when the displacement gradients are small such that $||\mathbf{H}|| \ll 1$, where $||\cdot||$ is the tensor norm. Given small displacement gradients, the Green–Lagrange strain tensor, $\mathbf{E}$, is equal to the infinitesimal strain tensor such that $\mathbf{E} = \frac{1}{2}(\mathbf{H} + \mathbf{H}^{\mathrm{T}}) + \mathscr{O}(||\mathbf{H}||^2)$

Furthermore, we posit that the vascular wall tissues for both the artery and the vein are elastic materials whose stress tensors can be described in terms of their respective strains, i.e., $\mathbf{S} = \mathbf{S}(\mathbf{E})$, where $\mathbf{S}$ is the second Piola–Kirchhoff stress tensor. For small strain, the stress can be expanded in a Taylor series about zero Green–Lagrange strain such that

$$\begin{aligned}\mathbf{S}(\mathbf{E}) &= \mathbf{S}\big|_{\mathbf{E}=\mathbf{0}} + \left.\frac{\partial \mathbf{S}}{\partial \mathbf{E}}\right|_{\mathbf{E}=\mathbf{0}} :\mathbf{E} + \mathscr{O}(||\mathbf{E}||^2) \\ &= \mathbf{T}_o + \mathbb{C}:\mathbf{E} + \mathscr{O}(||\mathbf{E}||^2). \end{aligned} \tag{1}$$

where

$$\mathbf{T}_o \equiv \mathbf{S}\big|_{\mathbf{E}=\mathbf{0}} \tag{2}$$

is the pre-stress tensor, and

$$\mathbb{C} \equiv \left.\frac{\partial \mathbf{S}}{\partial \mathbf{E}}\right|_{\mathbf{E}=\mathbf{0}} \tag{3}$$

is the tangent elasticity tensor. The first Piola–Kirchhoff stress, $\mathbf{P}$, is therefore given by

$$\begin{aligned}\mathbf{P} &= (\mathbf{I} + \mathbf{H}) \cdot \mathbf{S} \\ &= (\mathbf{I} + \mathbf{H}) \cdot (\mathbf{T}_o + \mathbb{C}:\mathbf{E}) + \mathscr{O}(||\mathbf{H}||^2) \\ &= \mathbf{T}_o + \mathbf{H} \cdot \mathbf{T}_o + \mathbb{C}:\mathbf{E} + \mathscr{O}(||\mathbf{H}||^2) \\ &= \mathbf{T}_o + \mathbf{E} \cdot \mathbf{T}_o + \boldsymbol{\Omega} \cdot \mathbf{T}_o + \mathbb{C}:\mathbf{E} + \mathscr{O}(||\mathbf{H}||^2) \\ &= \mathbf{T}_o + (\mathbf{I} \underline{\otimes} \mathbf{T}_o + \mathbb{C}):\mathbf{E} + (\mathbf{I} \underline{\otimes} \mathbf{T}_o):\boldsymbol{\Omega} + \mathscr{O}(||\mathbf{H}||^2) \end{aligned} \tag{4}$$

where $\boldsymbol{\Omega} = \frac{1}{2}(\mathbf{H} - \mathbf{H}^{\mathrm{T}})$ is the infinitesimal rotation tensor and the product $(\mathbf{M} \underline{\otimes} \mathbf{N})_{ijkl} = M_{ik}\, N_{jl}$ for arbitrary second-order tensors $\mathbf{M}$ and $\mathbf{N}$. This expression for the first Piola–Kirchhoff stress is consistent with previous analyses (Baek et al. 2007) based on the theory of "small-on-large" deformations in that the stress can depend on small strains, small rotations, and the pre-stress tensor.

Regarding the linearity of the material, evidence suggests that peripheral artery tissue can be approximated as linear over the range of deformations of the normal cardiac cycle based on ex vivo pressure/diameter measurements (Baek et al. 2007) of the basilar artery. Veins, on the other hand, are typically much more deformable than arteries under normal venous conditions (Widmaier et al. 2006). However, under the arterial-like conditions of an AV fistula, where the internal pressure is much greater than that of the venous circulation, experiments suggest that *veins are much less compliant than arteries at the same pressures*. Above 30 mmHg, the veins of the peripheral circulation, such as the saphenous (Dobrin et al. 1988) or the jugular (Kritharis et al. 2010), become increasingly stiff and are much less compliant than corresponding arteries under the same pressures. Therefore, we treat the venous tissue behavior as linear under the current conditions given their relatively low distensibility.

For the material elasticity tensor, $\mathbb{C}$, we suggest that the same constitutive equation be used for both the arterial and venous tissue of the fistula. However, we do not assume that the material constants are the same for the different tissues. In each case, we assume that the tangent elasticity tensor is described by an isotropic Saint Venant–Kirchhoff-like material such that

$$\mathbb{C} = \lambda_s \, \mathbf{I} \otimes \mathbf{I} + \mu_s \, \mathbf{I}^s \tag{5}$$

where λ_s and μ_s are (Lamé-like) material constants and $\mathbf{I}^s$ is the symmetric fourth-order identity tensor.

Several of the terms appearing in Eq. 4 can additionally be neglected as they are "small." For example, the stresses arising from rotations can be neglected as they are small relative to the stresses arising from strains, i.e., $\left|\left|\left(\mathbf{I} \underline{\otimes} \mathbf{T}_o\right) : \boldsymbol{\Omega}\right|\right| \ll \left|\left|\mathbb{C} : \mathbf{E}\right|\right|$ (Baek et al. 2007). Likewise, the second term on the right-hand side of Eq. 4, i.e., the strain tensor contracted into the pre-stress tensor, is also hypothesized to be small, i.e., $\left|\left|\mathbf{I} \underline{\otimes} \mathbf{T}_o\right|\right| \ll \left|\left|\mathbb{C}\right|\right|$. This assumption will be justified in Sect. 3.2 below. Therefore, the first Piola–Kirchhoff stress tensor can be written as

$$\mathbf{P} = \mathbf{T}_o + \mathbf{P}', \quad \text{where} \quad \mathbf{P}' = \mathbb{C} : \mathbf{E} \tag{6}$$

for all subsequent analyses unless otherwise stated. In this case, $\mathbf{P}'$ is symmetric due to the symmetries of both $\mathbb{C}$ and $\mathbf{E}$.

Additional simplifications are made so that the material parameters can be easily obtained from the ultrasound-acquired wall motion measurements by a basic analysis. The vessels, both the artery and the vein, are assumed to be thin walled and cylindrically shaped. In addition, it is assumed that there is some pre-stress, $\mathbf{T}_o$ within the vessel at the mean (i.e., time-averaged) internal pressure, P_o, with a given mean radius, R_o, and mean wall thickness, h_o, and that the deformation of the wall is quasi-static. Then, the instantaneous pressure, P, and radial displacements, η_r are related by

$$\frac{(P - P_o)\, R_o}{h_o} = \left(2\frac{P_o\, R_o}{h_o} + 4\mu_s\right)\frac{\eta_r}{R_o}. \tag{7}$$

A derivation of this expression is given in Appendix 6.

2.2 Fluid computational method

The 3D Navier–Stokes equations are solved using ANSYS FLUENT (Release 12.1, ANSYS, Inc. Cannonsburg, PA), a finite-volume-based solver. Briefly, this technique divides the total fluid domain into small, but finite, control volumes within which the fluid problem is reformulated as an integral statement describing the fluid velocity, $\mathbf{u}$, and fluid pressure, p. For the Jth control volume, with a volume V_J and surface area A_J, the governing fluid equations for mass and momentum become

$$\int_{A_J} \mathbf{u} \cdot \mathbf{n}_J \, \mathrm{d}A = 0 \tag{8}$$

$$\frac{\partial}{\partial t}\int_{V_J} \rho^f \, \mathbf{u} \, \mathrm{d}V + \int_{A_J} \rho^f \left(\mathbf{u} \otimes \mathbf{u}\right) \cdot \mathbf{n}_J \, \mathrm{d}A = - \int_{A_J} p \, \mathbf{n}_J \, \mathrm{d}A + \int_{A_J} \mu \nabla \mathbf{u} \cdot \mathbf{n}_J \, \mathrm{d}A \tag{9}$$

where $\mathbf{n}_J$ is the outward unit normal vector of control volume J, ρ^f is the fluid density, and μ is the dynamic viscosity. The blood is treated as an incompressible and Newtonian fluid with a density of $1{,}050.0\,\mathrm{kg/m^3}$ and a dynamic viscosity of $3.5 \cdot 10^{-3}$ Pa · s (Lee and Steinman 2007). A second-order upwind scheme is used for the spatial discretization of the advective flux term in Eq. 9, while a central difference scheme is used to evaluate the viscous flux term (Hirsch 2007). The pressure term is spatially discretized using a weighted central difference. The time integration is done by a second-order pressure-implicit-splitting of operators (PISO) scheme which is a type of projection method. The PISO scheme also enforces the incompressibility of the flow at each time step. The geometry is discretized with a semi-structured tetrahedral mesh, using the package ANSYS® GAMBIT® (Release 2.4, ANSYS, Inc.). The tetrahedral volumes have a characteristic width of 150 μm. The number of computational cells in the fluid model is 6.23 million.

At the inflow artery, an unsteady Womersley velocity profile with one mean and seven harmonic components is prescribed as the fluid boundary condition. The prescribed flow profile temporal behavior is determined from the in vivo centerline velocity (Womersley 1955) as measured by the Doppler ultrasound. At the outflow boundaries, Γ_i, a traction condition is prescribed for the flow such that

$$p = P_i, \quad \text{and} \quad \frac{\partial \mathbf{u}}{\partial n} = 0 \quad \text{on} \quad \Gamma_i \tag{10}$$

where P_i is the prescribed boundary pressure.

Two-element Windkessel (i.e., resistance-capacitance) models are used to determine the boundary pressure, P_i. In vivo measurements of fistula outflow vein impedance show that it is well approximated by a single resistive element up to $\approx$ 10 Hz (Schwartz et al. 1991). However, two-element models are used here as they are more numerically stable. The Windkessel models are integrated in time by a fully implicit second-order backward difference formula as described previously (McGah et al. 2013). The Windkessel elements are manually calibrated to achieve outflow rates consistent with the in vivo Doppler ultrasound-derived flow rates. The in vivo venous flow rate is calculated by multiplying the cross-sectional averaged Doppler ultrasound velocity by the cross-sectional area of the vessel. This technique gives an uncertainty in the in vivo flow rate of $\approx \pm 13\,\%$ (Zierler et al. 1992). Flow rate in the distal artery is calculated by applying a mass balance through the fistula and asserting that the time-averaged flow rates must all sum to zero.

2.3 Structural computational method

The structural dynamic equations for linear momentum are solved by the displacement formulation of the finite element method with an in-house code. The weak (Galerkin method) form of the structural equations written in the reference configuration becomes

$$\int_{\Omega_o^s} \rho^s\, \mathbf{w}\cdot\ddot{\boldsymbol{\eta}}\, \mathrm{d}V + \int_{\Omega_o^s} \nabla_o \mathbf{w} : \mathbf{P}\, \mathrm{d}V = \int_{\Gamma_o^N} \mathbf{w}\cdot\mathbf{t}_o\, \mathrm{d}A + \int_{\Omega_o^s} \mathbf{w}\cdot\mathbf{b}\, \mathrm{d}V \tag{11}$$

where ρ^s is the density of the vessel wall, $\mathbf{w}$ is the weighting function, $\mathbf{b}$ is a body force within the structure, Ω_o^s is the domain of the structure, and Γ_o^N is the portion of the boundary where tractions are prescribed. The structure is also assumed to be thin walled, in which case, the tractions on the lumen interface will be transmitted uniformly through the thickness of the vessel (Figueroa et al. 2006) such that the lumen traction acting on the structure, $\mathbf{t}^L$, can be related to the body force as

$$\mathbf{b} = \frac{\mathbf{t}^L}{h^s} \tag{12}$$

where h^s is the structure thickness. The volume integrals can be converted into 2D surface integrals since the structure is thin and its properties do not vary across the thickness. The weak form for the thin-walled structure is

$$\int_{\Gamma_o^L} \rho^s\, h^s\, \mathbf{w}\cdot\ddot{\boldsymbol{\eta}}\, \mathrm{d}A + \int_{\Gamma_o^L} h^s\, \nabla_o \mathbf{w} : \mathbf{P}'\, \mathrm{d}A = \int_{\Gamma_o^L} \mathbf{w}\cdot\mathbf{t}^L\, \mathrm{d}A - \int_{\Gamma_o^L} h^s\, \nabla_o \mathbf{w} : \mathbf{T}_o\, \mathrm{d}A \tag{13}$$

where Γ_o^L represents the luminal boundary. Boundary conditions for the wall displacements need only be prescribed on the inlet and outlet "rings." For this study, zero displacement, or clamped, boundary conditions are enforced.

The displacements of the vessel walls are represented with linear membrane triangular elements augmented with transverse shears. Only the three translational, but no rotational, degrees of freedom are needed to describe the solid motion with these elements (Figueroa et al. 2006). The membrane condition is usually justified by the fact that the cardiac pressure wavelength is $\mathcal{O}(1\,\mathrm{m})$, but the vessel diameters are $\mathcal{O}(1\,\mathrm{mm})$. In the local coordinate system of the element, $\mathbf{x}^l$, let the z direction represent the through thickness coordinate. In the membrane state, the out-of-plane normal stress is zero, i.e., $\mathbf{P}^l_{zz} \approx 0$, and the out-of-plane derivatives are zero, i.e., $\frac{\partial}{\partial z} \approx 0$. Thus, there are only five independent components for the local stress and strain, i.e., $\mathbf{P}'^l = \left\{P_{xx},\ P_{yy},\ P_{xy},\ P_{xz},\ P_{yz}\right\}^{\mathrm{T}}$ and $\mathbf{E}^l = \left\{E_{xx},\ E_{yy},\ E_{xy},\ E_{xz},\ E_{yz}\right\}^{\mathrm{T}}$. The local element strains are related to the local nodal displacements, $\boldsymbol{\eta}^l$, by the expression

$$\mathbf{E}^l = \mathbf{B}\,\boldsymbol{\eta}^l \tag{14}$$

where $\mathbf{B}$ is a matrix operator containing the spatial derivatives of the shape functions (Hughes 2000).

Invoking the symmetries of the stress and strain tensors, one can use a reduced second-order tensor to represent the tangent elasticity tensor, which for a thin-walled problem takes the form (Hughes 2000)

$$\mathbf{P}'^l = \mathbf{C}^l\,\mathbf{E}^l \tag{15}$$

where

$$\mathbf{C}^l = \begin{bmatrix} \bar{\lambda}+2\mu_s & \bar{\lambda} & 0 & 0 & 0 \\ \bar{\lambda} & \bar{\lambda}+2\mu_s & 0 & 0 & 0 \\ 0 & 0 & 2\mu_s & 0 & 0 \\ 0 & 0 & 0 & 2\mu_s & 0 \\ 0 & 0 & 0 & 0 & 2\mu_s \end{bmatrix} \tag{16}$$

and where

$$\bar{\lambda} = \frac{2\mu_s\lambda_s}{\lambda_s+2\mu_s}.$$

The solid is treated as incompressible, in which case the first Lamé-like parameter is very large, i.e., $\lambda_s \gg \mu_s$, such that $\bar{\lambda} \approx 2\mu_s$. Also note that a Lagrange multiplier does not need to be incorporated into the stress tensor to enforce the incompressibility as the structure is thin walled.

Given Eq. 16, the individual element stiffness matrix is constructed in the local coordinate system and then rotated into the global coordinate system where each element matrix is assembled into the global stiffness matrix (Hughes 2000). Similarly, the global mass matrix and the global element force vector, representing the luminal tractions, are also constructed in a local frame before rotation and assembly. However, consider the pre-stress tensor in Eq. 13. The pre-stress in the vascular wall arises to counteract the background hydrodynamic pressure in the vessel acting on the structure so that structural equilibrium is maintained. Therefore, the pre-stress term in Eq. 13 is assumed to be balanced with the traction on the lumen arising from the time-averaged background pressure, namely that

$$\int_{\Gamma_o^L} h^s \, \nabla_o \mathbf{w} : \mathbf{T}_o \, \mathrm{d}A = \int_{\Gamma_o^L} \mathbf{w} \cdot \bar{\mathbf{t}}^{\,L} \, \mathrm{d}A \tag{17}$$

where $\bar{\mathbf{t}}^{\,L}$ is the time-averaged luminal traction.

2.4 Fluid–structure coupling

Since structural displacements are assumed to be small, a fixed Eulerian frame is used to describe the fluid domain and lumen interface. Small, but non-zero, transpiration velocities are imposed as boundary conditions onto the fluid arising from the lumen motion (Deparis et al. 2003; Figueroa et al. 2006). The transpiration boundary conditions between the fluid and structure along the lumen boundary, Γ_o^L, are

$$\mathbf{u} = \dot{\boldsymbol{\eta}} \tag{18}$$

$$\boldsymbol{\sigma}^f \cdot \mathbf{N}_s = \mathbf{t}^L \tag{19}$$

where $\boldsymbol{\sigma}^f$ is the fluid Cauchy stress tensor and $\mathbf{N}_s$ is the outward unit normal of the structure.

A segregated solution algorithm is used for the fluid–structure coupling whereby the fluid and structure equations are solved separately but are continually iterated at each time step until convergence is achieved below some specified tolerance. The structural time-stepping is accomplished with a trapezoidal rule. An under-relaxation of the structural displacements is used to alleviate numerical instabilities which afflict segregated solutions strategies (Causin et al. 2005). Briefly, let $\boldsymbol{\eta}_{k+1}^*$ be the pre-relaxed structural displacement at the $k+1$ iteration for the $n+1$ time step. The "relaxed" displacement of the structure is therefore

$$\boldsymbol{\eta}_{k+1}^{n+1} = \omega \boldsymbol{\eta}_{k+1}^* + (1-\omega)\boldsymbol{\eta}_k^{n+1} \tag{20}$$

and ω is the relaxation parameter, which is less than one. Additionally, the fictitious mass technique of Baek and Karniadakis (2012) for segregated solutions is also used to aid in convergence. The fictitious mass acts to "slow down" the structure's motion but does not affect the overall system dynamics once a converged solution is achieved. The convergence of the system is judged by monitoring the L_2 norm of the change in vessel wall displacements such that

$$\frac{1}{\sqrt{N_{nd}}} \left\| \boldsymbol{\eta}_{k+1}^* - \boldsymbol{\eta}_k^{n+1} \right\|_2 < \mathrm{TOL} \tag{21}$$

where N_{nd} is the total number of structural nodes and TOL is the specified convergence tolerance.

The tractions from the fluid solution are imposed onto the structure at each iteration, while the velocities of the structure are imposed as boundary conditions onto the fluid at each iteration. The solid and fluid meshes are perfectly matched at the lumen, so no special interpolation scheme is needed. There are about 177 thousand elements within the structure, corresponding to about 266 thousand structural degrees of freedom. The overall algorithm is presented as pseudocode in Algorithm 1.

Algorithm 1 FSI Coupling

```
Start
for n = 1 to n = n_max do {Time Step Loop}
  for k = 1 to k = k_max do {FSI Loop}
    Impose Structure Velocity, v_k^{n+1}, on Fluid Boundary
    Update Fluid Velocity, u_{k+1}^{n+1}, and Pressure p_{k+1}^{n+1}
    Calculate Fluid Tractions on Lumen
    Update Structure Displacement, η*_{k+1}
    Relax Structure Displacement, i.e., equ. 20, obtain η_{k+1}^{n+1}
    Update Structure Velocity, v_{k+1}^{n+1}
    if Structure Converged, i.e., equ. 21 then
      Break
    else
      k = k + 1
    end if
  end for{End FSI Loop}
  n = n + 1
end for{End Time Step Loop}
```

The FSI coupling has been verified for unsteady flow in a straight elastic tube. More thorough details of both the finite element solution validation as well as the coupling algorithm can be found in McGah (2012).

3 Results

3.1 Fistula characteristics

The 3D reconstruction of the fistula is shown in Fig. 1 with the suture line delineating the portions into "arterial" or "venous" tissue. The total length of the vascular model for the fistula is about 75 mm. The diameters of the reconstructed proximal artery, distal artery, and outflow vein are 4.68, 2.68, and 7.96 mm, respectively. The period of the cardiac cycle is 0.85 s.

The in vivo flow rate, as measured by Doppler ultrasound, in the proximal artery has a mean of 652 mL/min and a max of

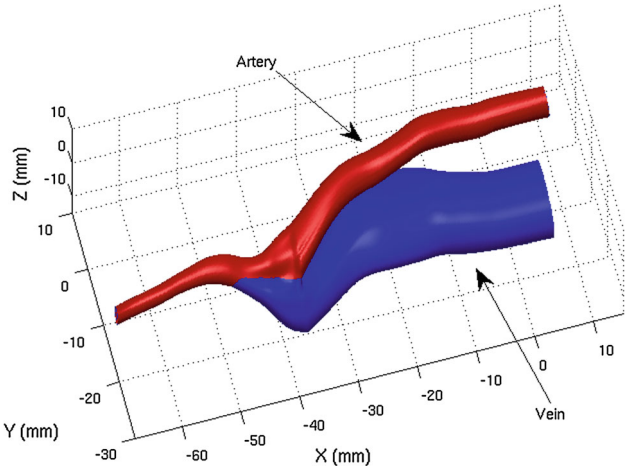

Fig. 1 Fistula 3D reconstruction. *Red color* denotes arterial lumen, and *blue color* denotes venous lumen. The orientation of the model is such that the skin is toward the $-z$ direction

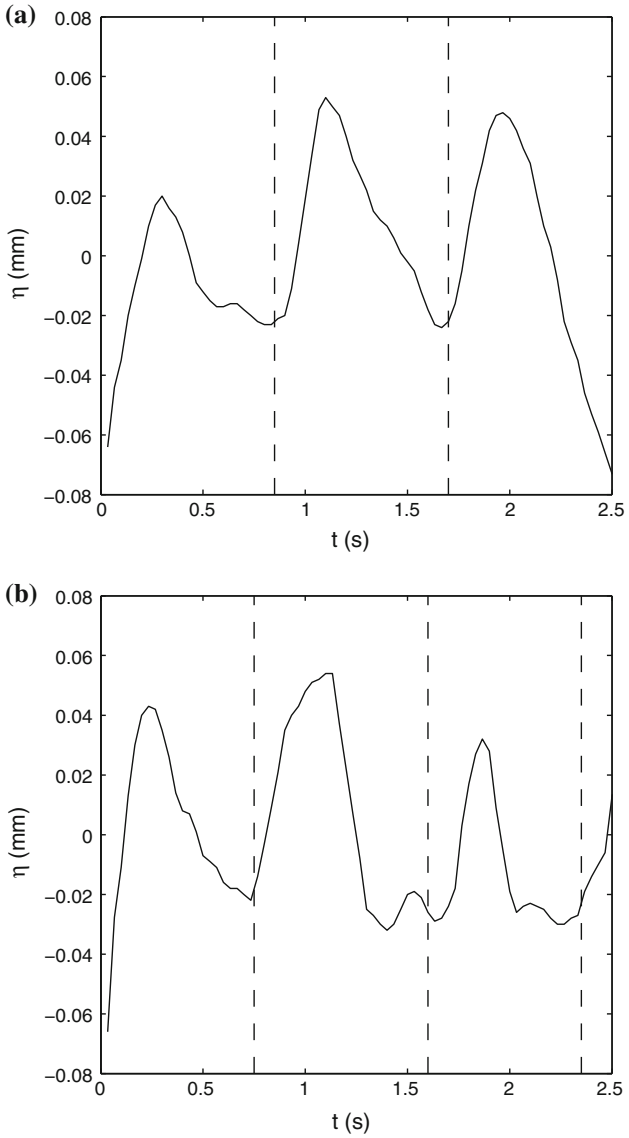

Fig. 2 In vivo wall motion measurements over three cardiac cycles. Radial displacement versus time for **a** proximal artery and **b** proximal vein. *Vertical dashed line* delineate individual cardiac cycles

1041 mL/min. The flow rate in the proximal vein has a mean of 630 mL/min and a max of 989 mL/min. The venous flow rate is higher than the minimum required for adequate dialysis, $>$ 250 mL/min (Wong et al. 1996). The patient's blood pressure, measured with a sphygmomanometer on the upper arm opposite of the fistula, is 132/56 mmHg. The mean arterial pressure is approximated by adding 1/3 of the difference between the systolic and diastolic pressures to the diastolic value, which in this case results in a mean arterial pressure of 81 mmHg. Note that it is typical for patients with AV fistulae to have such low diastolic pressures (Corpataux et al. 2002). The venous pressure is estimated by subtracting from the arterial values the pressure drops which were calculated in prior rigid-walled simulations (McGah et al. 2013) of the same fistula. In this case, the venous pressure is 127, 79, and 55 mmHg for the systolic, mean, and diastolic pressure, respectively.

3.2 Wall motion measurements

The arterial wall motion was recorded by ultrasound about 35 mm proximal to the anastomosis, $x \approx 0$ in Fig. 1, while the venous wall motion was recorded about 80 mm proximal to the anastomosis, not included in the 3D reconstruction. Both measurements are taken at points with an orientation facing toward the skin. The mean diameter of the artery is 4.64 mm with a wall thickness of 0.55 $\pm$ .07 mm. Maximum systolic diameter is 4.73 $\pm$ .04 mm (mean $\pm$ standard deviation, three cardiac cycles) corresponding to maximum circumferential strain of 1.97 %. The mean diameter of the proximal vein is 7.68 mm with a wall thickness of 0.51 $\pm$ .07 mm. Maximum systolic diameter is 7.84 $\pm$ .02 mm (mean $\pm$ standard deviation, three cardiac cycles) corresponding to a maximum circumferential strain of 1.16 %. The measured strains justify the use of a small strain assumption over the cardiac cycle motion for the full FSI computations. Time-dependent in vivo wall displacements are shown in Fig. 2.

Invoking Laplace's law, see Eq. 27 in Appendix 6, for the mean circumferential wall stress in a thin-walled vessel, and using the mean pressure of 81 mmHg, the mean wall stress in the proximal artery is computed as $T_{o,\theta\theta} = 45.6$ kPa. Using a mean pressure of 79 mmHg in the proximal vein, the mean wall stress is computed as $T_{o,\theta\theta} = 80.9$ kPa.

Seven unique data points are used to determine the elastic parameters for each vessel: three maximum systolic displacements and four minimum diastolic displacements. The pressure is assumed to be the same at each systole or diastole in each cardiac cycle. Solving Eq. 7 for the arterial conditions

Table 1 Wall mechanical properties derived from in vivo measurements

	Proximal artery	Proximal vein
Radius, R_o (mm)	2.32	3.88
Wall thickness, h_o (mm)	0.55	0.51
Mean circumferential stress, $T_{o,\theta\theta}$, (kPa)	45.6	80.9
Max. circumferential strain, $E_{\theta\theta}$, (%)	1.97	1.16
Incremental elastic modulus, μ_s, (kPa)	272 ± 64	780 ± 95

gives the modulus μ_s as 272 ± 64 kPa (mean $\pm$ standard error of the mean). For the venous conditions, the modulus μ_s is calculated as 780 ± 95 kPa (mean $\pm$ standard error of the mean). The standard errors associated with the tangent moduli are also taken as a measure of the random uncertainty in the wall measurements. Wall properties are summarized in Table 1.

It was stated without proof in Sects. 2.1 and 2.3 that several terms in the expression for the stress tensor can be neglected so that Eq. 4 can be reduced to Eq. 6. Justification is provided here based on an order of magnitude analysis. The following scales are used for the terms that appear in Eq. 4 for either the arterial or venous tissue, respectively:

$$\begin{aligned} ||\mathbf{T}_o|| &\sim T_{o,\theta\theta}, \qquad ||\mathbf{I} \underline{\otimes} \mathbf{T}^o|| \sim T_{o,\theta\theta} \\ ||\mathbb{C}|| &\sim 4\mu_s, \qquad ||\mathbf{E}|| \sim E_{\theta\theta} \\ ||(\mathbf{I} \underline{\otimes} \mathbf{T}_o) : \boldsymbol{\Omega}|| &\sim T_{o,\theta\theta} \cdot E_{\theta\theta}, \qquad ||\mathbb{C}:\mathbf{E}|| \sim 4\mu_s \cdot E_{\theta\theta}. \end{aligned}$$

The scale for the pre-stress tensor, $T_{o,\theta\theta}$, is taken to be the mean circumferential stress, while the scale for the strain, $E_{\theta\theta}$, and rotation is taken to be the maximum circumferential strain. Both quantities are given in Table 1.

Based on these estimates, the dyadic product of the pre-stress is small compared to the tangent elasticity tensor, i.e., $||\mathbf{I} \underline{\otimes} \mathbf{T}^o|| \ll ||\mathbb{C}||$, since $T_{o,\theta\theta} \ll 4\mu_s$. The ratio of the pre-stress to the tangent modulus is 2.6 and 4.2 % for the vein and the artery, respectively. A similar argument can be made to neglect the stresses occurring due to rotations, namely that $||(\mathbf{I} \underline{\otimes} \mathbf{T}_o) : \boldsymbol{\Omega}|| \ll ||\mathbb{C}:\mathbf{E}||$ since $T_{o,\theta\theta} \cdot E_{\theta\theta} \ll 4\mu_s \cdot E_{\theta\theta}$, giving the same order of magnitude estimate as above. However, the total pre-stress is not negligible relative to the tangent stiffness, i.e., $||\mathbf{T}_o|| \sim ||\mathbb{C}:\mathbf{E}||$ since $T_{o,\theta\theta} \sim 4\mu_s \cdot E_{\theta\theta}$.

3.3 FSI computations

The material properties and the thickness of the vein are assumed to be spatially uniform over the whole vein. Likewise, the modulus and thickness of the artery wall are assumed spatially uniform over the whole artery. This implies that there is a "jump discontinuity" in the both the wall thickness and the tangent modulus along the anastomosis suture line. The density of the artery and venous tissue is set equal to $1{,}200.0\ \mathrm{Kg/m^3}$. The background fluid pressure is taken to be a constant of 80 mmHg.

3.3.1 Algorithm controls

A time step of $\Delta t = .001$ s is used for the FSI simulation, corresponding to 850 time steps per cardiac cycle. The mesh size, $\approx 150\ \mu$m, and time step size were determined in previous work (McGah et al. 2013) to resolve the wall shear stress to within 5 % of a grid-independent solution estimated using a Richardson extrapolation. The fictitious mass parameter for the structure solution is set equal to 10.0. The under-relaxation factor, ω, in Eq. 20, is set equal to 0.1. The relative residual tolerances in the fluid subiterations for mass and momentum are set to $\leq 10^{-5}$. At each time step, the convergence is found to be limited by the displacement of the wall. The wall residual tolerance, Eq. 21, is set to $\leq 10^{-8}$ m, corresponding to a relative residual of $\sim 10^{-4}$. Convergence of the wall displacements required between 20 to 30 FSI iterations, "k" index in Algorithm 1, in order to achieve the necessary error tolerance. These convergence criteria are found a posteriori to limit the error in the global (i.e., integral over the domain) mass balance to $\leq 2 \cdot 10^{-4}$ relative to the mean arterial inflow rate.

The resistance and capacitance of the distal artery Windkessel model are $R = 3.10 \cdot 10^{10}\ \mathrm{Pa \cdot s/m^3}$ and $C = 2.567 \cdot 10^{-13}\ \mathrm{m^3/Pa}$, respectively. The resistance and capacitance of the proximal vein are $R = 9.80 \cdot 10^{8}\ \mathrm{Pa \cdot s/m^3}$ and $C = 8.120 \cdot 10^{-12}\ \mathrm{m^3/Pa}$, respectively.

3.3.2 Solution initialization

The velocity and the pressure of the fluid from the previous rigid wall simulation are used as the initial conditions for the FSI simulation. The flow and pressure are taken from the phase of the cardiac cycle during the systolic acceleration when the surface-averaged lumen pressure is close to the value of 80 mmHg which was chosen in order to minimize the initial forcing, and hence acceleration, of the structure. The unsteady FSI simulation is then started with zero displacement and zero velocity for the structure. Two cardiac cycles are completed and then discarded from the analysis to eliminate initial transients.

3.4 FSI results

Simulated proximal arterial pressure is 122/47 mmHg (systolic/diastolic) with a mean of 79 mmHg. This compares favorably with the in vivo measurements: 132/56 mmHg with mean of 81 mmHg measured in the brachial artery contralateral to the fistula. The simulated pressure in the proximal vein

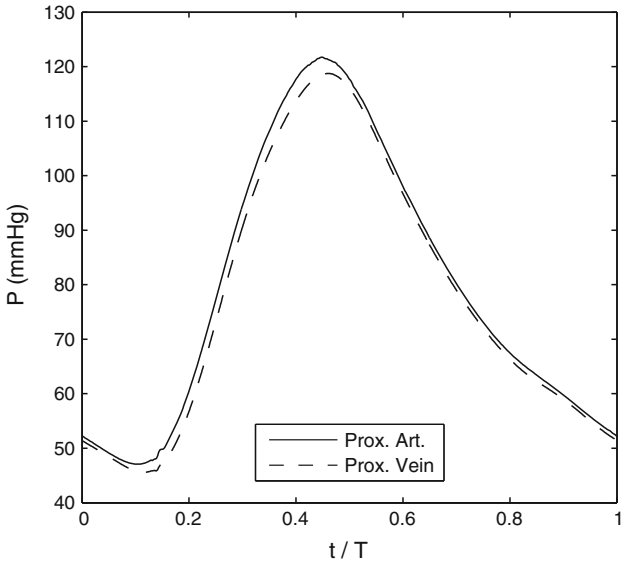

Fig. 3 Simulated pressure versus time on the boundaries of the proximal artery (Prox. Art.) and proximal vein (Prox. Vein)

at the domain outflow is 119/46 mmHg with a mean venous pressure of 77 mmHg. The temporal history of the pressures on the venous outflow boundary and arterial inflow boundary is shown in Fig. 3.

The distensibility of the walls allows for storage of a volume of blood within the computational domain. Therefore, the shape and the phase of the venous outflow rate are altered compared to its rigid counterpart. The FSI simulation computed a maximum venous flow rate of 971 mL/min and a time average of 636 mL/min. For comparison, the rigid simulation (McGah et al. 2013) computed a maximum flow rate of 1,012 mL/min and a time average of 632 mL/min. The venous outflow rates for the rigid and FSI simulations are shown in Fig. 4a.

The capacitance of the blood vessels does cause the expected phase lag in the venous flow rate. A temporal lag of 0.039 s (phase angle of 16.7°) is computed between the rigid and FSI cases for the phase of maximum venous flow rate. The mass flux across the outer faces of the fluid mesh elements on the lumen surface, which equates to the rate of instantaneous mass storage, is shown in Fig. 4b. The storage rate has a maximum of 173 mL/min and a minimum of −102 mL/min which is about 15 % of the total flow through the fistula. The characteristic velocities of the vessel wall are $\mathcal{O}(1$ mm/s).

3.5 Simulated wall displacements

The time signals of the computed displacements at spatial points can be compared to the ultrasound measured in vivo wall displacements in order to validate the FSI simulation. Although this comparison is "circular," in that in vivo displacements have already been used to obtain the vessel material constants, the comparison still shows that the simulation produces wall motions which are consistent with the in vivo conditions and thus justifies our modeling assumptions.

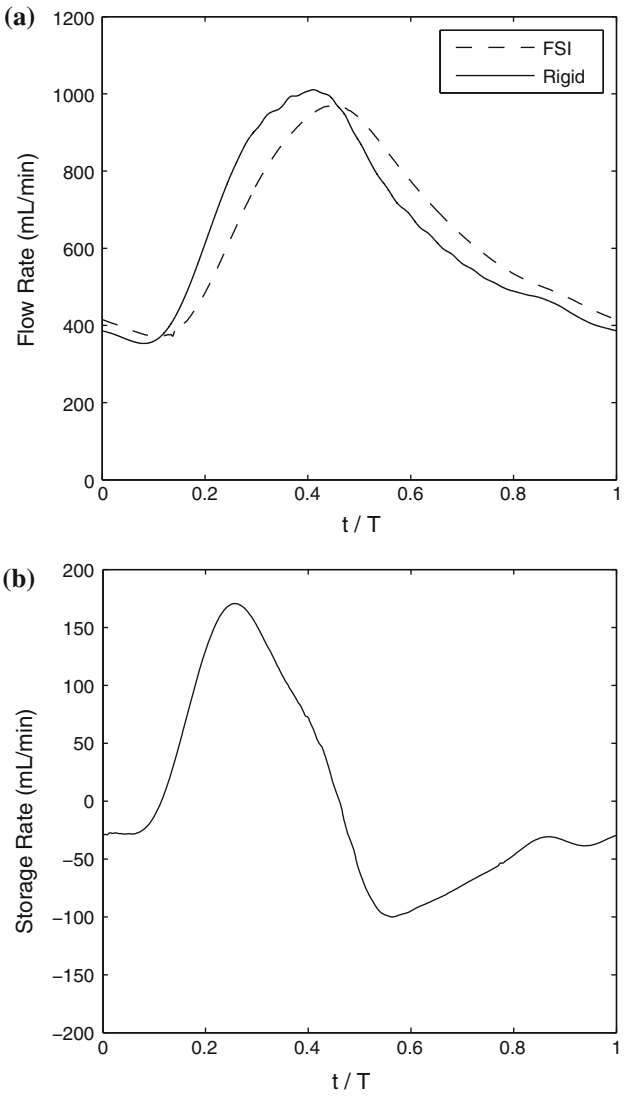

Fig. 4 Flow rates versus time **a** venous outflow rates for the rigid and FSI simulation **b** Rate of blood storage in the fistula due to the distensibility of the wall

The mechanical strain is computed within the vessel wall during a post-processing step. We use the second invariant of the strain tensor, $\mathrm{II}(\mathbf{E})$, as a measure of total strain in the wall which, for an incompressible material undergoing small deformations, is $||\mathbf{E}|| \equiv \sqrt{-\mathrm{II}(\mathbf{E})} = \sqrt{\frac{1}{2} E_{ij}\, E_{ij}}$. The maximum simulated strain at peak systole is located at the "apex" of the anastomosis and is equal to 5.3 %. There is a jump in the strain between the two tissues along the suture line. The mean maximum systolic strain in the elements immediately adjacent to the suture line is 3.00 % on the arterial side and is

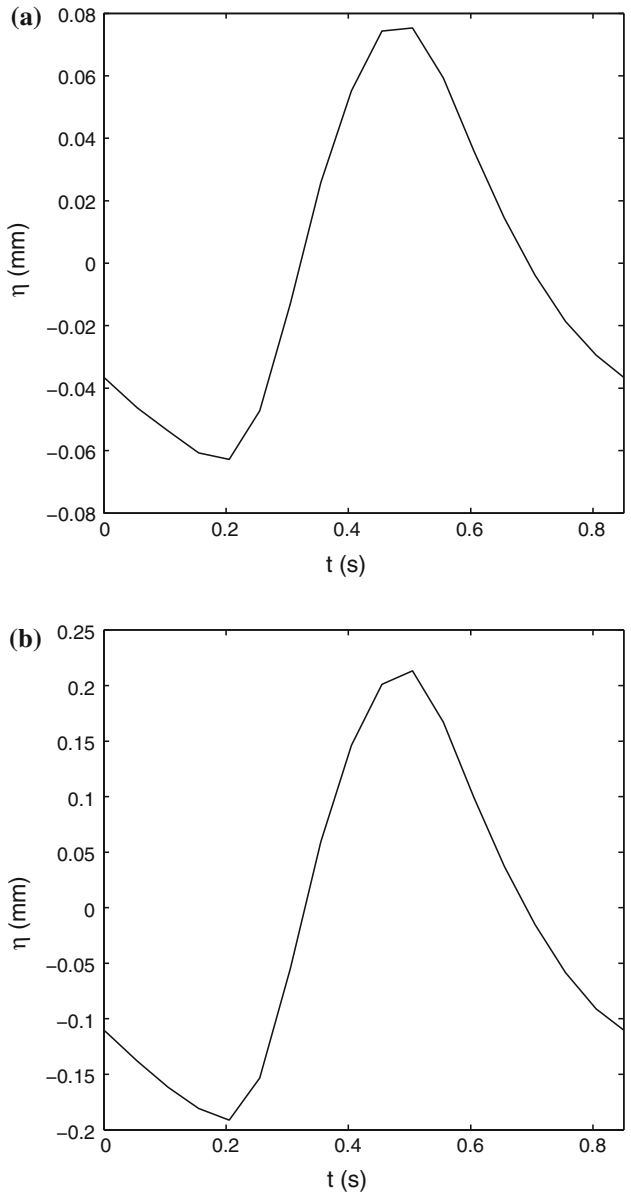

Fig. 5 Simulated wall-normal displacements versus time **a** Arterial displacements and **b** Venous displacements

1.41 % on the venous side. Interestingly, the vein is normally assumed (Ballyk et al. 1998) to suffer more from abnormal stress concentrations due to the compliance mismatch at the suture as veins are typically less stiff than arteries. However, that is not the case in this fistula due to the larger stiffness of the vein under arterial pressures. Caution must be considered when interpreting this result as the internal wall stress computations may not be precise given the simplifications and assumptions of the material model (e.g., constant wall thicknesses or isotropic material).

Figure 5a plots the wall-normal simulated **arterial** displacements versus time at a single material point. The material point is located at the same position both in silico along the vessel axis at $x \approx 0.5$ mm on the proximal artery and in vivo in the ultrasound-acquired measurements. Positive displacement is toward the surface of the skin. The in vivo measurements recorded three cardiac cycles, while the simulation only recorded one cardiac cycle. Modest agreement is found between the two data sets, e.g., compare with 2a. Peak in vivo displacement are 45.7 ± 17.3 μm (mean ± SD, three cycles), and a minimum displacement of -51.1 ± 22.8 μm. The simulation computed a maximum displacement of 75.3 μm and a minimum displacement of -62.8 μm.

Figure 5b plots the wall-normal **venous** displacement versus time at an arbitrary, but typical, material point located at $x \approx -1.5$ mm. Positive displacement is toward the surface of the skin. However, the in vivo measurement is located at a point over 50 mm farther proximal, which is beyond the end of the model domain. The ultrasound system measured peak displacement of 43.0 ± 11.0 μm and minimum displacement of -42.3 ± 17.0 μm, i.e., see Fig. 2b. The simulation computed a maximum venous displacement of 213 μm and a minimum venous displacement of -191 μm. Possible reasons for the large discrepancy are discussed below in Sect. 4.

As an additional validation of the simulation, we compare the strains computed in the FSI simulation to the strains directly calculated form the ultrasound measurements (previously given in Table 1). The maximum strain magnitude occurring at the material point on the artery shown in Fig. 5a is 2.32 %. In comparison, the maximum circumferential strain calculated directly from the ultrasound measurements is 1.97 %. Similarly, the maximum strain occurring at the material point on the vein shown in Fig. 5b is 1.16 %, while the maximum circumferential stress calculated directly from the ultrasound measurements is 1.12 %. The FSI simulation is therefore computing vessel strains consistent with the in vivo measurements.

3.6 Wall shear stresses

The time-averaged viscous wall shear stresses computed in the FSI case are compared with those in the rigid-wall case reported previously (McGah et al. 2013). Exact definitions of the instantaneous and time-averaged wall shear stress are given in Appendix 7. To facilitate easy comparison between the two cases, the lumen is divided up into small, nearly equal-sized rectangular "patches" using the surface mapping and patching feature in the Vascular Modeling Toolkit, or VMTK (www.vmtk.org). The average size of a patch is 10.40 mm^2, and the total number of patches is 264. The time-averaged wall shear stress is spatially averaged within each patch for all cases. The rigid and FSI cases also use the same patching topology.

The majority of the flow entering the fistula through the proximal artery must make a 180° turn as it leaves through the proximal vein. In both the rigid and FSI cases, the blood

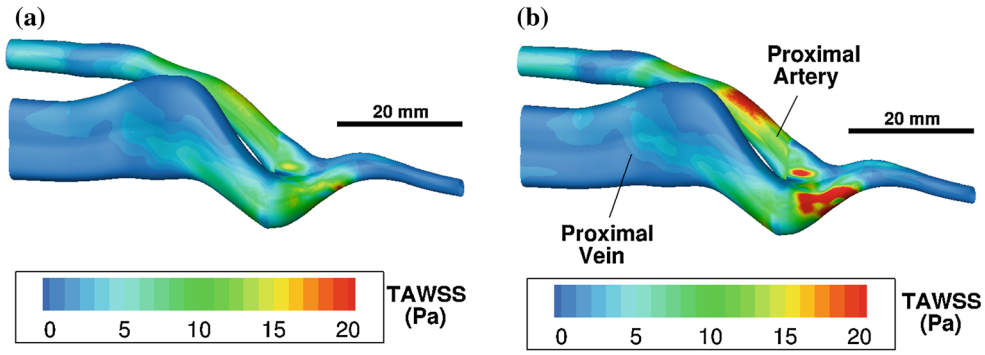

Fig. 6 Time-averaged wall shear stress maps on the fistula lumen in Pa. Subfigures (**a**) and (**b**) show results from the rigid and FSI cases, respectively. The view is looking from the skin toward the fistula. The large value of the shear stress on the anastomosis is due to the flow impingement

flow entering through the proximal artery impinges onto the distal side of the anastomotic wall. This produces a stagnation point-like flow and results in very high shear stresses on a ring around the stagnation point at the anastomosis. Instantaneous systolic shear stresses exceed 20 Pa, and time-averaged shear stresses exceed 10 Pa at the anastomosis in both cases. Figure 6 shows the time-averaged wall shear stress for (a) the rigid case and (b) the FSI case. Strong secondary flows and vortices are generated near the stagnation point and are advected downstream into the outflow vein. The venous flow stabilizes a few centimeters downstream of the anastomoses as the vortices tend to decay.

The data for the patched shear stress data are presented in Figs. 7 and 8 as a "limits of agreement" plot where each data point represents the shear stress at a given patch location. The FSI case systematically predicts lower shear stresses compared to the rigid case. The differences have a clear downward

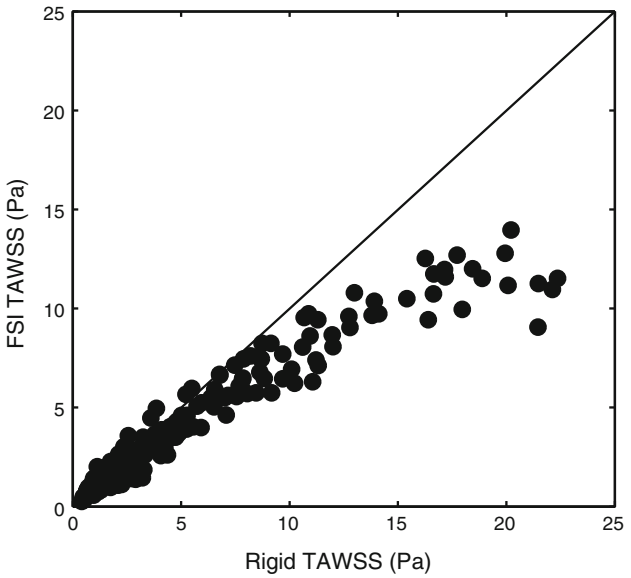

Fig. 7 Agreement plot of time-averaged shear stress on lumen patches of rigid versus FSI cases. *Dots* represent data from individual patches, while the *solid line* is the identity line

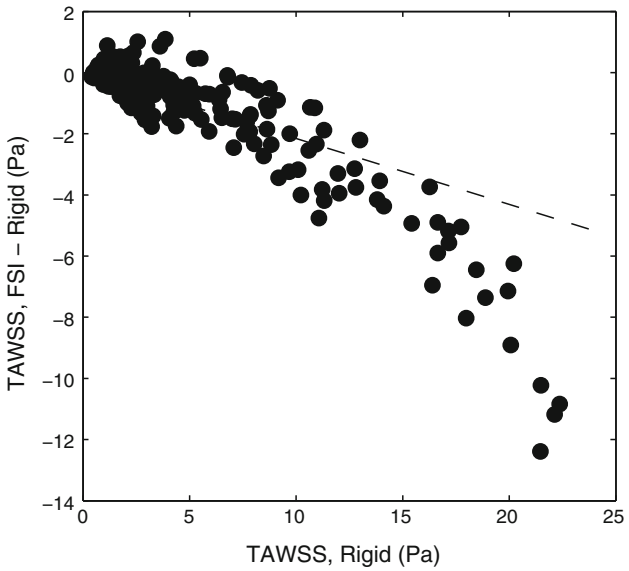

Fig. 8 Limits of agreement plot of time-averaged shear stress on lumen patches between rigid and FSI cases. The abscissa is the shear stress computed in the rigid case, and the ordinate is the difference in the time-averaged shear stress between the FSI and rigid cases. *Dots* represent data from individual patches, while *dashed line* represents the average systematic trend of $\approx -21.5\,\%$

trend with increasing shear stress. Spatially averaging the time-averaged wall shear stress across all patches yields an averaged value of 3.81 Pa for the rigid case and 2.98 Pa for the FSI case and an average difference of 0.820 Pa, or $-21.5\,\%$. The largest absolute difference is located on the anastomotic lumen near the flow stagnation point where the FSI predicts a patch time-averaged wall shear stress of 9.01 Pa, or $\approx 58\,\%$ lower than the rigid case, 21.46 Pa, on the same patch. For patches located on the anastomosis, the FSI, on average, predicts the time-averaged wall shear stress as $37.7\,\%$ lower than the rigid simulation. Farther away from the anastomosis, > 5 mm, the relative differences are not as large: average differences are $11.4\,\%$ for the outflow vein, $20.4\,\%$ for the proximal artery, and $17.4\,\%$ for the distal artery. At the segments farthest from the anastomosis, > 20 mm, the absolute

values of the time- and- space-averaged wall shear stress over each vessel segment are as follows: 1.19 Pa for the outflow vein, 3.66 Pa for the proximal artery, and 0.92 Pa for the distal artery.

Although the FSI simulation computed lower shear stress than that of the rigid case, the magnitude of the wall shear stress on the anastomotic lumen is still much larger than what is considered the normal homeostatic value in the peripheral vasculature. In mature radiocephalic AV fistulae used for dialysis access, the normal homeostatic time-averaged wall shear stress has been reported between 2.5 and 4.0 Pa (Dammers et al. 2005; Ene-Iordache et al. 2003) in the feeding radial artery and as 1.0 Pa (Corpataux et al. 2002) in the draining cephalic vein, which are based on Doppler ultrasound measurements. In the same studies (Dammers et al. 2005; Ene-Iordache et al. 2003), the maximum radial artery wall shear stress has been reported between 4.0 and 7.0 Pa. Here, however, time-averaged wall shear stress at the anastomosis flow stagnation point are computed as 10–15 Pa for the FSI case and as 15–25 Pa in the rigid case. These values are an order of magnitude higher than what is typically considered homeostatic in the cephalic vein. However, the current results are roughly in agreement with more recent hemodynamic simulations of mature human (Carroll et al. 2011) and porcine models (Krishnamoorthy et al. 2008) of AV fistulae which reported very high wall shear stresses, > 20 Pa, on fistulae anastomoses.

A scalar quantity, "the highly stressed area," given by Eq. 35 in Appendix 7, is computed for the FSI simulation. The highly stressed area is a scalar value which has been used previously (McGah et al. 2013) to quantify the extent of the lumen which is exposed to some arbitrary, but large, threshold value of instantaneous shear stress. A comparison of the computed highly stresses area, A_τ, using different values of shear thresholds for both the rigid and FSI cases is shown in Fig. 9. The highly stressed area data are normalized with the square of the proximal artery diameter, D_A. The differences between the rigid and FSI cases becomes greater as a higher shear stress threshold is chosen. Using a threshold of 7.5 Pa gives normalized highly stressed areas of 17.3 (rigid) and 17.1 (FSI). Yet, using a threshold of 15 Pa gives a larger difference with normalized highly stressed areas of 6.73 (rigid) and 3.09 (FSI). Despite a systematic reduction compared to the rigid case, the FSI simulation still predicts that a significant portion of the anastomosis is subjected to instantaneous wall shear stress greater than 15 Pa, about 2-3 times greater than what is typically considered the normal maximum wall shear stress.

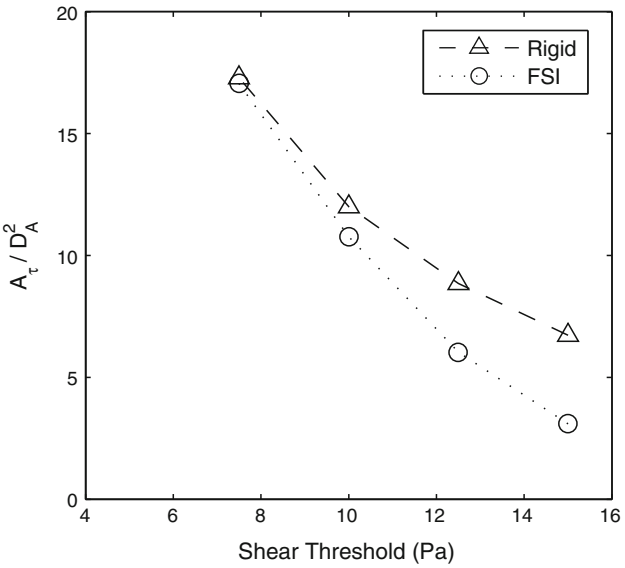

Fig. 9 Highly stressed area, A_τ, normalized by the proximal artery diameter, D_A, using different values of the shear threshold for both the rigid and FSI cases

4 Discussion

Although the qualitative picture of the wall shear stress on the arterial and venous sides of the AV fistula outlined by the rigid wall and FSI simulations is consistent, there are quantitative differences in the time-averaged wall shear stress predictions between the rigid and FSI simulations. Differences at the anastomosis are as high as 50 %, while differences at the proximal vessels away from the anastomosis are less pronounced: about 10 % in the proximal vein and about 20 % in the proximal artery. The shear stress predicted by the FSI simulation is nearly always lower than the result from rigid simulations. This is the expected behavior: in a distensible wall simulation, the vessel can "yield" and reduce the velocity gradient at the lumen interface. Poiseuille's law shows that the shear rate is inversely related to the cube of the vessel diameter (assuming that the flow rate is constant). Therefore, a 2 % increase in the vessel diameter would reduce the wall shear stress by about 6 %.

The results of Figs. 7, 8 and 9 show that the distensibility attenuates the higher wall shear stresses more so than lower magnitudes. This suggests a relative indifference of the results between rigid wall and FSI simulations at high shear magnitudes. There are also small differences in the highly stressed area, A_τ in Fig. 9, using the lowest value of wall shear stress threshold, in this case 7.5 Pa, which is several times the normal physiological shear stress in peripheral vessels. The mechanosensitive response of the endothelium at these stress levels would be saturated; shear-dependent endothelial nitric oxide production has been shown to asymptote to a constant level at $\geq$5 Pa in steady flow in vitro experiments of bovine aortic endothelial cells (Metaxa et al. 2008). Fully accurate values of wall shear stress, particularly high values, may have a minor effect when incorporated into theoretical models of vessel growth and remodeling as the shear

stress "dose-response" relationship saturates above this certain threshold.

If one considers the opposite, that is that the response of the vascular tissue to the values above these thresholds is important, then the lower shear stress predictions may be important. For example, if endothelial signaling is sensitive to values of shear stress between 10 and 20 Pa, then the computation of lower stresses with FSI simulations points to significant challenges in predicting the wall remodeling in AV fistula. Certainly more work is needed to understand the mechanobiological response of vascular endothelial cells under such extreme shear stress conditions occurring in AV fistulae.

4.1 Utility of rigid-wall simulations

Other authors have reported large reductions in wall shear stress computations between FSI and rigid hemodynamic simulations. In one of the first computational studies of cardiovascular fluid–structure interaction in 1995, Perktold and Rappitsch (1995) reported relative differences of 25 % in wall shear stress in a distensible and rigid idealized model of the carotid bifurcation. A more recent study of Bazilevs et al. (2009) performed FSI simulations in a patient-specific model of the vena cava and pulmonary arteries after the Fontan procedure. Their FSI simulations predicted wall shear stresses 15–20 % lower than the corresponding rigid simulations. The differences were most pronounced at vessel bifurcations. These relative reductions in shear stress are roughly in agreement with the results reported here.

Some investigators, such as Bazilevs et al. (2009), have suggested that it is therefore necessary to incorporate wall distensibility in order to accurately predict the wall shear stress. Others, such as Lee and Steinman (2007), have suggested that the error in wall shear stress introduced by a rigid assumption is minor relative to the uncertainties such as the reconstruction of the vessel and prescription of flow rates; errors in the wall shear stress due to the geometric reconstruction have been reported to be as high as 30–40 %. Thus, it is argued that wall distensibility is of secondary importance given current levels of geometric precision and the complexity of FSI simulations.

The results of the FSI here do cast a degree of uncertainty onto the results of a previous study (McGah et al. 2013) of rigid-walled simulations. Nevertheless, the overall conclusions of the rigid-wall analysis are still justified by the FSI analysis. Very high wall shear stresses ($>10-15$ Pa), well above what is typically considered the homeostatic point, are still observed at the anastomosis in the FSI simulations. Although the extent of high wall shear stresses is reduced in the FSI results, the high stresses nonetheless persist. Therefore, the inclusion of distensible vessel walls does not reduce the very high values wall shear stress in AV fistulae to "normal" levels.

Yet, despite the abnormally high shear stresses, the fistula showed no stenoses and was clinically patent at the time of the ultrasound examination. At least in this single case, it appears the fistula can be subjected to wall shear stresses well above the normal homeostatic value without its clinical patency being compromised. This finding is, however, in contrast to previous hypotheses (Carroll et al. 2011; Misra et al. 2008) regarding the role of hemodynamic shear stress in AV fistula failure. More work is needed to articulate the role of very high wall shear stress in the growth and remodeling of the outflow vein in AV fistulae.

Furthermore, it is hypothesized here that the hemodynamic *trends across the patients* derived from the rigid simulations may be valid, even if the absolute values are systematically altered. This hypothesis would support the use of rigid-walled hemodynamic analyses as it still can provide valuable information as part of a screening mechanism for patients at risk of fistula failure. Rigid-wall analyses could still be used to calculate relative risk across patients which could correlate to important clinical outcomes.

4.2 The mechanism of wall shear stress reduction

The large reduction in wall shear stress in the FSI simulation for regions at or near the anastomosis is much higher than what would be expected due to the effect of increased vessel diameter alone based on Poiseuille's law; with maximum displacements at the anastomosis of 5 %, one would expect reductions in shear of 15 %. We therefore conjecture that an additional hemodynamic mechanism attenuates the wall shear stresses near the anastomosis: vessel wall motion changes the thickness of the viscous boundary layer occurring at the flow impingement point. The fluid in the impinging jet is redirected radially outward from the stagnation point along the distal wall of the anastomosis. A thin viscous boundary layer develops on the anastomosis between the fast radially outward motion of the flow jet and the slow fluid near the lumen wall (due to the no-slip condition). In rigid-wall simulations, there is a sharp velocity gradient, and hence shear stress, across this boundary layer that partially accounts for the increased shear around the anastomosis stagnation point. In the FSI simulations, the wall motion introduces a small "transpiration" velocity at the anastomosis wall. The added momentum transfer between the outer fluid jet and the fluid near the anastomosis wall will thicken the boundary layer and lessen the velocity gradient, reducing the shear stress.

4.3 Agreement of wall displacement measurements

The simulation predicts arterial wall displacements which agree only modestly against in vivo measurements. Predicted displacements on the proximal artery are almost 50 %

higher than the in vivo measurements. Although the *relative* error between the simulated and in vivo may seem large, the *absolute* error between the two is nevertheless small. The difference in the maximum arterial displacement between the simulated and in vivo results is 29.6 μm. This is a very minor difference relative to the additional length scales of the problem such as the radius of the proximal artery (≈ 2.3 mm).

An important source of error is the elastic modulus uncertainty, ≈ 25 %. The large cycle-to-cycle variations in the ultrasound-derived diameters also make the determination of a reference radius, needed for defining displacement, more difficult. The wall thickness measurements also contain random uncertainties (10–15 %) which are also not accounted for in the standard errors of the elastic moduli shown in Table 1. Additional discrepancies may also be due in part to the choice of boundary conditions of the FSI simulation. The basic in vivo analysis assumed that the vessel was very long such that axial strain was negligible. However, the end effects of the wall motion do produce non-negligible axial strain. The axial strain was about 10 % relative to the circumferential strain at peak systole at the chosen simulated material point. In addition, the analysis of the in vivo measurements assumed the vessel was a straight, cylindrical shape. The 3D reconstruction of the lumen is not perfectly circular, nor perfectly straight, which also introduces additional sources of error.

For the venous wall displacements, the difference between the simulated and in vivo data was even larger; the simulation predicts displacements a factor of 5 larger than the in vivo measurements. The comparisons are made at two different material points on the vein, as the point for the ultrasound-derived motion was not included in the 3D reconstruction. Although one would not expect quantitative agreement between the displacements measured at points that are so distant with respect to the anastomoses, more than 50 mm apart, there are still several important sources of error to be discussed. The disagreement may first be due to parametric uncertainty, for example in the elastic modulus. Secondly, the cross-sectional shape of the vein in the FSI model is highly elliptic, whereas the in vivo measurements are made in a segment where the vein cross-section is more circular. The shape of the cross-section can strongly influence vessel stiffness and displacement. The simulation data are extracted at a point on the major, or wider, side of the vessel, which would have a larger local radius of curvature and thus, a smaller local mechanical stiffness resulting in larger displacements.

Nevertheless, the simulations predict maximum wall strains for both the artery and the vein which are in better agreement with the ultrasound-derived values. In light of this, the FSI simulations do reasonably produce the low-frequency wall motion associated with the cardiac cycle. Even still, the current FSI simulations tended to predict displacements which are higher than the in vivo values. Thus, the FSI analysis may even exaggerate the influence of wall distensibility on the hemodynamics.

4.4 Study limitations

First, this study examines only one patient model, and the results may not be easily generalizable to larger cohorts of patients. There is a clear systematic under-prediction of wall shear stress, shown in Figs. 8 and 9, for this single patient, but it is unknown how variable this trend is across patients. Certainly, studies with a larger number of patients are needed to ensure robust correlations.

Second, this study does not include longitudinal information of the fistula's natural history and progression. It is not known whether significant remodeling was occurring either immediately before or after the time of our ultrasound examination. Nonetheless, such an occurrence would seem unlikely given that the fistula was over seven years old and fully functioning at the time of the examination as remodeling after the initial 12–16 week period is rare.

Third, the material model used here is simple and should be improved upon in future studies. Although the simulation produces reasonable displacements, there is less certainty about its ability to predict accurate stress distributions. More realistic constitutive equations incorporating material anisotropy and heterogeneity or variable wall thicknesses are needed to accurately describe the state of stress at a complicated shape such as an anastomosis.

Lastly, the coupling algorithm, specifically the under-relaxation scheme, should be improved upon in future FSI simulations of AV fistulae. The rate of convergence of the fluid–structure iterations is particularly slow, which led to the choosing of a large value of the structural density, $1{,}200\,\mathrm{kg/m^3}$, in order to speed up computational time. Better methods, such as (quasi)-Newton iterations, should be incorporated to ensure an efficient, but also robust, numerical solution.

5 Conclusions

In this study, we have presented results of a fully coupled fluid–structure interaction numerical simulation of an arteriovenous fistula, the first of its kind in the open literature. Ultrasound measurements of in vivo vessel wall motion are used to validate the simulations ability to predict displacements of the low-frequency vessel motion due to the propagation of the arterial pressure wave. The FSI simulations predicted systematically lower time-averaged wall shear stresses compared to the analogous rigid-walled simulations. Nonetheless, the predicted time-averaged wall shear stress at the fistula anastomosis in the FSI simulation is still very large, $>10-15\,\mathrm{Pa}$, much larger than what is typically

considered normal in the peripheral arteries and veins. The results of a previous analysis (McGah et al. 2013) of AV fistulae using rigid-wall boundary conditions, which also predicted very large wall shear stresses on the anastomoses, are likely still justified as the inclusion of distensible vessel walls in hemodynamic simulations does not reduce the high anastomotic shear stresses to "normal" values.

Furthermore, we would agree with Lee and Steinman (2007) in that rigid-walled image-based hemodynamic simulations can still be justified in certain contexts as the current uncertainties in the geometric reconstruction may outweigh the complexity of including wall distensibility. In this context, rigid simulations can still predict values of wall shear stress within the same order of accuracy of the FSI equivalent simulations. Along a similar line of thought, rigid-wall simulations may still be justifiable, and clinically useful, if the results are used to establish relative risks across patients. Nevertheless, distensible walls are certainly necessary in other contexts such as understanding the physical mechanisms associated with thrills and bruits in dialysis access vessels (Lee et al. 2005).

Acknowledgments The authors would like to thank Dr. Suhail Ahmad and Lori Linke at the Scribner Kidney Center (Northwest Kidney Centers, Seattle, WA) for their assistance with the imaging studies of the dialysis patients and Edward Stutzman of UW Vascular Surgery for help performing the ultrasound examinations. The authors would also like to thank Ultrasonix Medical Corporation for the use of their SonixTouch ultrasound scanner for the patient imaging studies.

6 Derivation of simplified wall motion equations

The first Piola–Kirchhoff stress, Eq. 4, and the the Cauchy stress in the solid, $\mathbf{T}$, are related to each other by the expression

$$\mathbf{T} = \frac{1}{J}\,\mathbf{P}\cdot\mathbf{F}^{\mathrm{T}} \tag{22}$$

where $\mathbf{F}$ is the deformation gradient tensor and J is the determinant of the deformation gradient tensor, which for an incompressible material is equal to 1. Multiplying Eq. 4 through by the transpose of the deformation gradient, and assuming small deformations, we obtain

$$\begin{aligned}\mathbf{T} &= \left(\mathbf{T}_o + \mathbf{E}\cdot\mathbf{T}_o + \boldsymbol{\Omega}\cdot\mathbf{T}_o + \mathbb{C}{:}\mathbf{E}\right)\cdot\left(\mathbf{I}+\mathbf{H}^{\mathrm{T}}\right) + \mathscr{O}\left(||\mathbf{H}||^2\right)\\ &= \mathbf{T}_o + \mathbf{E}\cdot\mathbf{T}_o + \mathbf{T}_o\cdot\mathbf{E} + \mathbb{C}{:}\mathbf{E} + \boldsymbol{\Omega}\cdot\mathbf{T}_o - \mathbf{T}_o\cdot\boldsymbol{\Omega} + \mathscr{O}\left(||\mathbf{H}||^2\right)\\ &= \mathbf{T}_o + \left(\mathbf{I}\underline{\otimes}\,\mathbf{T}_o + \mathbf{T}_o\,\overline{\otimes}\,\mathbf{I} + \mathbb{C}\right){:}\mathbf{E}\\ &\quad + \left(\mathbf{I}\underline{\otimes}\,\mathbf{T}_o + \mathbf{T}_o\,\overline{\otimes}\,\mathbf{I}\right){:}\,\boldsymbol{\Omega} + \mathscr{O}\left(||\mathbf{H}||^2\right)\end{aligned} \tag{23}$$

and where the tensor product $(\mathbf{M}\overline{\otimes}\mathbf{N})_{ijkl} = M_{il}\,N_{jk}$ for arbitrary second-order tensors $\mathbf{M}$ and $\mathbf{N}$.

For the simplified analysis, we assume that the fistula vessels are thin-walled cylinders undergoing a quasi-static and axisymmetric inflation over the cardiac cycle. The axial strains, E_{zz}, can be assumed to be much smaller than the circumferential strains, $E_{\theta\theta}$ since the lengths of the vessels, ~100 mm, are much larger than the vessel radii, ~1 mm. Shear strains and stresses arising from rotations are zero for a simple inflation. Therefore, the circumferential stress, $T_{\theta\theta}$, and radial stress T_{rr} in terms of the strains are

$$T_{\theta\theta} = T_{o,\theta\theta} + \left(2\cdot T_{o,\theta\theta} + C_{\theta\theta\theta\theta}\right)E_{\theta\theta} + C_{\theta\theta rr}\,E_{rr} \tag{24}$$

$$T_{rr} = T_{o,rr} + \left(2\cdot T_{o,rr} + C_{rrrr}\right)E_{rr} + C_{rr\theta\theta}\,E_{\theta\theta}. \tag{25}$$

In the membrane state, the radial component of the stress is negligible such that $T_{rr} \approx 0$ and $T_{o,rr} \approx 0$ and the radial strains can be eliminated from the above equations such that

$$T_{\theta\theta} = T_{o,\theta\theta} + \left(2\cdot T_{o,\theta\theta} + \overline{C}_{\theta\theta\theta\theta}\right)E_{\theta\theta} \tag{26}$$

where $\overline{C}_{\theta\theta\theta\theta} = C_{\theta\theta\theta\theta} - \frac{C_{rr\theta\theta}C_{\theta\theta rr}}{C_{rrrr}}$. One can also invoke the law of Laplace for a thin-walled cylinder which relates the internal pressure within the vessel to the stress, in which case

$$T_{\theta\theta} = \frac{P\,R_o}{h_o} \tag{27}$$

$$T_{rr} = -\frac{P}{2} \tag{28}$$

which is a statically determinate state of stress for the cylinder. The circumferential strain for a long cylinder in terms of the radial deformations is simply $E_{\theta\theta} = \eta_r/R_o$. Thus, combining Eq. 26 with Eq. 27, and writing the strains in terms of displacements, one obtains

$$\frac{(P-P_o)\,R_o}{h_o} = \left(2\frac{P_o\,R_o}{h_o} + 4\mu_s\right)\frac{\eta_r}{R_o} \tag{29}$$

which is the expression previously given in Sect. 2.1.

7 Calculation of wall shear stress

The total wall viscous shear stress traction acting on the solid wall with unit normal in the current configuration, $\mathbf{n}_s$, is given as

$$\boldsymbol{\tau}(\mathbf{x},t) = \mu\left(\left(\nabla\mathbf{u}\right) + \left(\nabla\mathbf{u}\right)^{\mathrm{T}}\right)\cdot\mathbf{n}_s \tag{30}$$

where μ is the fluid viscosity. Given that the displacements are small, the unit normal in the current configuration can be approximated with the unit normal in the reference configuration, $\mathbf{N}_s$, such that

$$\mathbf{n}_s = \mathbf{N}_s + \mathscr{O}\left(||\mathbf{H}||\right).$$

The instantaneous wall shear stress is computed as the absolute value of the wall shear stress vector at position $\mathbf{x}$ and time t such that

$$\tau(\mathbf{x},t) = \left(\tau_s^2(\mathbf{x},t) + \tau_m^2(\mathbf{x},t)\right)^{1/2} \tag{31}$$

where τ_s and τ_m are the two components of the wall shear stress vector which are perpendicular to the wall-normal vector. The wall-normal component of the wall shear stress is neglected. The time-averaged wall shear stress, TAWSS, over n number of cardiac cycles is computed by

$$\mathrm{TAWSS}(\mathbf{x}) = \frac{1}{n \cdot T} \int_0^{n \cdot T} \tau(\mathbf{x}, t)\, \mathrm{d}t \tag{32}$$

where T is the period of the cardiac cycle.

Furthermore, we define a "wall shear stress duty factor," $DF(\mathbf{x})$, which quantifies the fraction of the cardiac cycle for which the wall shear stress is above a certain stress threshold as

$$DF(\mathbf{x}) = \frac{1}{n \cdot T} \int_0^{n \cdot T} \phi(\mathbf{x}, t)\, \mathrm{d}t \tag{33}$$

where

$$\phi(\mathbf{x}, t) = \begin{cases} 1 & \text{if} \quad \tau(\mathbf{x}, t) \geq \tau_o \\ 0 & \text{if} \quad \tau(\mathbf{x}, t) < \tau_o \end{cases} \tag{34}$$

and where τ_o is some shear stress threshold. The "highly stressed lumen area," A_τ, is then defined as

$$A_\tau = \int_A DF(\mathbf{x})\, \mathrm{d}A \tag{35}$$

where A is the luminal surface area. This is an arbitrary yet simple measure of high shear acting on the vessels. Since the duty factor can only range from 0 to 1, the stressed area is weighted by the length of time the wall shear is above the given threshold.

References

Baek S, Gleason RL, Rajagopal KR, Humphrey JD (2007) Theory of small on large: potential utility in computations of fluid-solid interactions in arteries. Comput Meth Appl Mech Eng 196:3070–3078

Baek H, Karniadakis GE (2012) A convergence study of a new partitioned fluid-structure interaction algorithm based on fictitious mass and damping. J Comput Phys 231(2):629–652

Ballyk PD, Walsh C, Butany J, Ojha M (1998) Compliance mismatch may promote graft-artery intimal hyperplasia by altering suture-line stress. J Biomech 31:229–237

Bassiouny HS, White S, Glagov S, Choi E, Giddens DP, Zarins CK (1992) Anastomotic intimal hyperplasia: mechanical injury or flow induced. J Vasc Surg 15(4):708–717

Bazilevs Y, Hsu M, Benson DJ, Sankaran S, Marsden AL (2009) Computational fluid-structure interaction: methods and application to a total cavopulmonary connection. Comput Mech 45(1):77–89

Carroll GT, McGloughlin TM, Burke PE, Egan M, Wallis F, Walsh MT (2011) Wall shear stresses remain elevated in mature arteriovenous fistulas: a case study. J Biomech Eng 133(2):021,003–1

Causin P, Gerbeau JF, Nobile F (2005) Added-mass effect in the design of partitioned algorithms for fluid-structure problems. Comput Meth Appl Mech Eng 194:4506–4527

Corpataux JM, Haesler E, Silacci P, Res HB, Hayoz D (2002) Low-pressure environment and remodelling of the forearm vein in Brescia-Cimino haemodialysis access. Nephrol Dial Transpl 17:1057–1062

Dammers R, Stifft F, Tordoir JHM, Hammeleers JMM, Hoeks APG, Kitslaar PJEHM (2003) Shear stress depends on vascular territory: comparison between common carotid and brachial artery. J Appl Physiol 94:458–489

Dammers R, Tordoir JHM, Kooman JP, Welten R, Hameleers JMM, Kitslaar P, Hoeks APG (2005) The effect of flow changes on the arterial system proximal to an arteriovenous fistula for hemodialysis. Ultrasound Med Biol 31(10):1327–1333

Deparis S, Fernandez MA, Formaggia L (2003) Acceleration of a fixed point algorithm for fluid-structure interaction using transpiration conditions. ESIAM: Math Model Numer Anal 37(4):601–616

Dixon BS (2006) Why don't fistulas mature? Kidney Int 70:1413–1422

Dobrin PB, Littooy FN, Golan J, Blakeman B, Fareed J (1988) Mechanical and histological changes in canine vein grafts. J Surg Res 44:259–265

Ene-Iordache B, Mosconi L, Antiga L, Bruno S, Anghileri A (2003) Radial artery remodeling in response to shear stress increase within arteriovenous fistula for hemodialysis access. Endothelium 10:95–102

Ene-Iordache B, Remuzzi A (2012) Disturbed flow in radial-cephalic arteriovenous fistulae for haemodialysis: low and oscillating shear stress locates the sites of stenosis. Nephrol Dial Transpl 27(1):358–368

Figueroa CA, Vignon-Clemente IE, Jansen KE, Hughes TJR, Taylor CA (2006) A coupled momentum method for modeling blood flow in three-dimensional deformable arteries. Comput Meth Appl Mech Eng 195:5685–5706

Gibson KD, Gilen DL, Caps MT, Kohler TR, Sherrard DJ, Stehman-Breen CO (2001) Vascular access survival and incidence of revisions: a comparison of prosthetic grafts, simple autogenous fisulas, and venous transposition fistulas from the United States Renal Data System Dialysis Morbidity and Mortality Study. J Vasc Surg 34(4):694–700

Girerd X, London G, Boutouyrie P, Jaques Mourad J, Safar M, Laurent S (1996) Remodeling of the radial artery in response to a chronic increase in shear stress. Hypertension 27:799–803

Gurtin ME, Fried E, Anand L (2010) The mechanics and thermodynamics of continua. Cambridge University Press, New York

Hirsch C (2007) Numerical computation of internal and external flows: the fundamentals of computational fluid dynamics, vol 1. Butterworth-Heinemann

Hughes TJR (2000) The finite element method: linear static and dynamic finite element analysis. Dover Publications, Inc., New York

Humphrey JD (2002) Cardiovascular solid mechanics: cells, tissues, and organs. Springer, New York

Humphrey JD (2008) Vascular adaptation and mechanical homeostasis at tissue, cellular, and sub-cellular levels. Cell Biochem Biophys 50:73–78

Kamiya A, Togawa T (1980) Adaptive regulation of wall shear stress to flow change in the canine carotid artery. Am J Physiol 239(1):H14–H21

Krishnamoorthy MK, Banerjee RK, Wang Y, Zhang J, Roy AS, Khoury SF, Arend LJ, Rudich S, Roy-Chaudhury P (2008) Hemodynamic wall shear stress profiles influence the magnitude and pattern of stenosis in a pig AV fistula. Kidney Int 74:1410–1419

Kritharis EP, Kakisis JK, Giagini AT, Manos T, Stergiopulos N, Tsangaris S, Sokolis DP (2010) Biomechanical, morphological and zero-stress state characterization of jugular vein remodeling in arteriovenous fistulas for hemodialysis. Biorheology 47:297–319

Lauvao LS, Ihnat DM, Goshima KR, Chavez L, Gruessner AC, Mills JL Sr (2009) Vein diameter is the major predictor of fistula maturation. J Vasc Surg 49(1499–14):504

Lee SW, Fischer PF, Loth F, Royston TJ, Grogan JK, Bassiouny HS (2005) Flow-induced vein-wall vibration in an arteriovenous graft. J Fluids Struc 20(6):837–852

Lee SW, Steinman DA (2007) On the relative importance of rheology for image-based CFD models of the carotid bifurcation. J Biomech Eng 129(2):273–279

Legget ME, Leotta DF, Bolson EL, McDonald JA, Martin RW, Li XN, Otta CM, Sheehan FH (1998) System for quantitative three-dimensional echocardiography of the left ventricle based on a magnetic-field position and orientation sensing system. IEEE Trans Biomed Eng 45(4):494–504

Leotta DF, Primozich JF, Beach KW, Bergelin RO, Strandness DE Jr (2001) Serial measurement of cross-sectional area in peripheral vein grafts using three-dimensional ultrasound. Ultrasound Med Biol 27(1):61–68

Leotta DF, Primozich JF, Beach KW, Bergelin RO, Zierler RE, Strandness DE Jr (2003) Remodeling in peripheral vein graft revisions: serial study with three-dimensional ultrasound imaging. J Vasc Surg 37(4):798–807

Leotta DF, Primozich JF, Lowe CM, Karr LN, Bergelin RO, Beach KW, Zierler RE (2005) Measurement of anastomosis geometry in lower extremity bypass grafts with 3-D ultrasound imaging. Ultrasound Med Biol 31(10):1305–1315

McGah PM, Leotta DF, Beach KW, Zierler RE, Aliseda A (2013) Incomplete restoration of homeostatic shear stress within arteriovenous fistulae. J Biomech Eng 135(1):011,005

McGah PM (2012) Biomechanical modeling of the peripheral cardiovascular system. PhD thesis, University of Washington

Metaxa E, Meng H, Kaluvala SR, Szymanski MP, Paluch RA, Kolega J (2008) Nitric oxide-dependent stimulation of endothelial cell proliferation by sustained high flow. Am J Physiol: Heart Circ Physiol 295:H736–H742

Misra S, Fu AA, Puggioni A, Karimi KM, Mandrekar JN, Glockner JF, Juncos LA, Anwer B, McGuire AM, Mukhopadhyay D (2008) Increased shear stress with upregulation of VEGF-A and its receptors and MMP-2, MMP-9, and TIMP-1 in venous stenosis of hemodialysis grafts. Am J Physiol: Heart Circ Physiol 294(5):H2219–H2230

Owens CD, Wake N, Kim JM, Hentschel D, Conte MS, Schanzer A (2010) Endothelial function predicts positive arterial-venous fistula remodeling in subjects with stage IV and V chronic kidney disease. J Vasc Access 11(4):329–334

Perktold K, Rappitsch G (1995) Computer simulation of local blood flow and vessel mechanics in a compliant carotid artery bifurcation model. J Biomech 28(7):845–856

Schwartz LB, Purut CM, O'Donohoe MK, Smith PK, Otto Hagan P, McCann RL (1991) Quantitation of vascular outflow by measurement of impedance. J Vasc Surg 14(3):353–363

Shemesh D, Goldin I, Berelowitz D, Zaghal I, Zigelman C, Olsha O (2007) Blood flow volume changes in the maturing arteriovenous access for hemodialysis. Ultrasound Med Biol 33:727–733

Taylor CA, Figueroa CA (2009) Patient specific modeling of cardiovascular mechanics. Ann Rev Biomed Eng 11:109–134

Tordoir JHM, Rooyens P, Dammers R, van der Sande FM, de Haan M, Yo TI (2003) Prospective evaluation of failure modes in autogenous radiocephalic wrist access for hemodialysis. Nephrol Dial Transpl 18:378–383

US Renal Data System (2012) USRDS 2011 Annual Data Report: Atlas of end-stage-renal-disease in the United States. Tech. rep, National Institutes of Health, National Institute of Diabetes and Digestive and Kidney Diseases, Bethesda

Widmaier EP, Raff H, Strang KT (2006) Vander's human physiology: the mechanisms of body function, 10th edn. McGraw-Hill, New York

Womersley JR (1955) Method for the calculation of velocity, rate of flow and viscous drag in arteries when the pressure gradient is known. J Physiol 127:553–563

Wong V, Ward R, Taylor J, Selvakumar S, How TV, Bakran A (1996) Factors associated with early failure of arteriovenous fistulae for haemodyialysis access. Eur J Vasc Endovascular Surg 12:207–213

Zarins CK, Zatina MA, Giddens DP, Ku DN, Glagov S (1987) Shear stress regulation of artery lumen diameter in experimental atherogenesis. J Vasc Surg 5:413–420

Zierler BK, Kirkman TR, Kraiss LW, Reiss WG, Horn JR, Bauer LA, Clowes AW, Kohler TR (1992) Accuracy of duplex scanning for measurement of arterial volume flow. J Vasc Surg 16(4):520–526